Dalton Transactions

ROYAL SOCIETY OF CHEMISTRY

PAPER

View Article Online
View Journal | View Issue

Cite this: *Dalton Trans.*, 2026, **55**, 4951

Crystal structure and physical properties of shchurovskyite-related $K_2CaCu_6O_2(PO_4)_4$

G. V. Kiriukhina, *[a,b] O. V. Yakubovich, [a] L. V. Shvanskaya [a] and A. N. Vasiliev [a,c]

Received 15th January 2026,
Accepted 26th February 2026

DOI: 10.1039/d6dt00109b

rsc.li/dalton

A new oxocuprate phosphate, $K_2CaCu_6O_2(PO_4)_4$, was obtained as tabular dark-green single crystals through flux-assisted high-temperature synthesis. It crystallizes in the space group *P*2/*c* and represents the centrosymmetric modification of the fumarolic arsenate mineral shchurovskyite, $K_2CaCu_6O_2(AsO_4)_4$. The crystal structure of the compound under study is characterized by the presence of large channels filled with potassium cations. Bond-valence energy landscape calculations based on structural data showed the probability of K^+ migration through the crystal structure along the *b* axis at an energy of 0.6 eV. $K_2CaCu_6O_2(PO_4)_4$ ordered into a canted antiferromagnetic state in two steps at T_{N1} = 22 ± 2 K and T_{N2} = 10 ± 1 K, as revealed by magnetization and specific heat measurements.

Introduction

The eruption of the Tolbachik volcano in 1975 resulted in the appearance of a huge number of new copper-based minerals of fumarolic origin.[1] Most of them are oxocuprate salts incorporating additional oxygen atoms, which are not part of the acid residue. The peculiar magnetic properties of these natural compounds stem from the Jahn–Teller effect, leading to the distortion of Cu^{2+}-centered polyhedrons and the formation of various configurations (square, tetrahedral, square-pyramidal, trigonal–bipyramidal, octahedral, and heptahedral) of the magnetically active cation. These distortions correlate with variations in the symmetry of the entire crystal structure and with the pronounced anisotropy of magnetic exchange interactions. Among the numerous fumarolic oxocuprate sulfates, the most promising for investigating physical properties are nabokoite, $KCu_6CuTeO_4(SO_4)_5Cl$;[2] atlasovite, $KCu_6FeBiO_4(SO_4)_5Cl$;[3] and elasmochloite, $Na_3Cu_6BiO_4(SO_4)_5$;[4] all possessing a square kagome magnetic network. This network attracts attention as a platform for elusive spin-liquid quantum ground state, the Holy Grail of modern condensed matter physics.[5] Adjacent to this family is fedotovite $K_2Cu_3O(SO_4)_3$,[6] in which the edge-shared tetrahedral spin clusters of Cu^{2+} ions form a one-dimensional array. It has been shown both experimentally and theoretically that an effective spin S = 1 cluster-based Haldane state is realized in this compound at low temperatures.[7,8] Urusovite, $CuAlAsO_5$, is a valence bond crystal with a quantum ground state,[9] while a short-range magnetic order has been established in ilinskite, $KCu_5O_2(SeO_3)_2Cl_3$,[10] and a long-range magnetic order sets in chloromenite, $Cu_9O_2(SeO_3)_4Cl_6$,[11] and averievite, $Cu_5V_2O_{10}(CsCl)$.[12]

Shchurovskyite, $K_2CaCu_6O_2(AsO_4)_4$, is one more fumarolic mineral[13] that serves as the archetype for a family with a complex Cu-based magnetic subsystem. Recently, a series of new shchurovskyite-related compounds have been synthesized using hydrothermal and chemical vapor transport methods.[14,15] However, the physical properties of shchurovskyite itself and its phosphate analogues have not been studied. Aksenov *et al.* reported that $Rb_2CaCu_6O_2(PO_4)_4$ evidenced the ferrimagnetic ground state with residual magnetization equal to 1/3 of saturation magnetization.[14] Herein, we report the flux-assisted high-temperature synthesis of a new potassium calcium oxocuprate phosphate, $K_2CaCu_6O_2(PO_4)_4$, structurally related to fumarolic shchurovskyite. The crystal structure of this compound was determined using single-crystal X-ray diffraction, its physical properties were experimentally characterized, and the K^+-ion conductivity was theoretically evaluated.

Crystal structure

The title phase was first obtained as a by-product during an attempt to synthesize $KNa_3Cu_7(PO_4)_6$ crystals (in press). Initial reagents K_2CO_3 (0.0156 g), Na_2CO_3 (0.0359 g), $(NH_4)_2HPO_4$ (0.1790 g), and $CuCl_2{\cdot}2H_2O$ (0.2695 g) were taken in a molar ratio of 1 : 3 : 12 : 14 (total 0.5 g), mixed with the same amount of KCl (0.5 g) used as a flux and then gradually heated up to 690 °C in a porcelain crucible. The new phase was obtained as tabular dark-

[a]*Lomonosov Moscow State University, Moscow 119991, Russia. E-mail: g-biralo@yandex.ru*
[b]*Korzhinskii Institute of Experimental Mineralogy RAS, Chernogolovka 142432, Russia*
[c]*National University of Science and Technology MISIS, Moscow 119049, Russia*

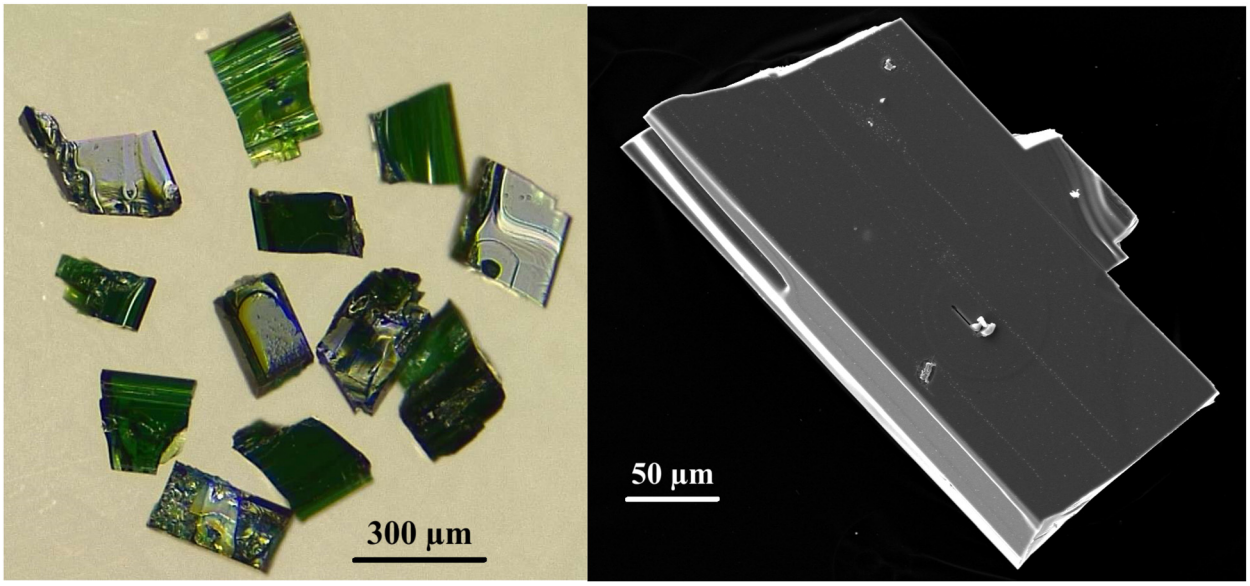

Fig. 1 Photograph (left) and SEM image (right) of the title phase.

green crystal concretions (Fig. 1). Isolated mechanically, high-quality crystals were subsequently used for further investigations by SEM and single-crystal X-ray diffraction.

To obtain a larger amount of the compound for magnetic measurements, targeted solid-state synthesis was performed. This time, K_2CO_3 (0.2317 g), $CaCO_3$ (0.1678 g), $CuCl_2{\cdot}2H_2O$ (1.7149 g), and $(NH_4)_2HPO_4$ (0.8856 g) were taken in stoichiometric proportions of 2 : 1 : 6 : 4 (total 3 g). The reagents were thoroughly mixed, ground, and gradually heated up to 870 °C, followed by slow cooling in three stages: first to 540 °C for 53 hours (5° per hour), then to 300 °C for 12 hours (12° per hour), and finally, to room temperature. A fine-crystalline dark-green product was obtained. According to the powder X-ray diffraction (PXRD) data, a minor impurity phase, $Ca_3Cu_3(PO_4)_4$, was detected, as shown in Fig. S1 of the (SI).

Crystals were mounted on a special plate, coated with carbon, and examined for their composition and homogeneity by energy-dispersive spectroscopy (EDS) using a JEOL JSM-IT500 scanning electron microscope (Laboratory of Analytical Techniques of High Spatial Resolution, Department of Petrology, Faculty of Geology, Lomonosov Moscow State University). The crystal morphology obtained by SEM is shown in Fig. 1. Semi-quantitative EDS analysis, performed on an unpolished sample under standard conditions (accelerating voltage = 20 kV, beam current = 10 nA, exposure time = 50 s), revealed the presence of K, Ca, Cu, P, and O in an atomic ratio of 1.6 : 0.9 : 5.9 : 4 : 17. NaCl, potassium feldspar ($KAlSi_3O_8$), metallic Cu, and GaP were used as reference standards.

A small dark-green crystal, selected using a binocular microscope, was examined by preliminary single-crystal X-ray diffraction. As its quality was good enough, it was used for full structural investigation. The data were collected using an Xcalibur (Oxford Diffraction) diffractometer equipped with Mo Kα radiation and corrected for Lorentz and absorption effects.[16] The crystal structure was solved by direct methods in the monoclinic space group $P2/c$ using the SHELXT program[17] and refined by full-matrix least-squares on F^2 using SHELXL,[18] both implemented in the WinGX software package.[19] During the refinement, partial cationic disorder was detected for potassium and calcium sites. The K1 and K2 positions were located 0.69(2) Å apart and refined with site occupancies of 0.21(2) and 0.79(2), respectively. Calcium was found to be isomorphically substituted by Cu^{2+} ions, with refined occupancies of 0.876(8) (Ca) and 0.124(8) (Cu). The final refinement converged to R = 0.038, yielding the formula $K_2(Ca_{0.876}Cu_{0.124})Cu_6O_2(PO_4)_4$, which is consistent with the elemental composition determined by EDS X-ray spectroscopy. Crystallographic data and refinement details are summarized in Table 1, and atomic coordinates with equivalent isotropic displacement parameters are listed in Table S1 of the SI. The crystal structure was visualized using the Diamond software.[20]

The crystal structure of the title compound consists of two symmetrically independent orthophosphate tetrahedra, four distinct copper coordination polyhedra, a calcium octahedron, and a large potassium polyhedron (Fig. 2). Both PO_4 groups exhibit the lowest symmetry (C_1) and typical P–O bond lengths ranging from 1.522(3) to 1.564(3) Å, with an average of 1.54 Å (Table S2 of the SI). Each phosphate tetrahedron shares all its vertices with copper or calcium polyhedra.

Copper cations occupy four crystallographically independent sites with distinct oxygen coordination environments. Cu1 and Cu2 atoms lie on twofold rotation axes at the 2f Wyckoff site, positioned one above the other along the b axis. The anionic coordination around Cu1 is octahedral, with two pairs of short Cu–O bonds of 1.925(3) and 1.960(3) Å and one pair of elongated bonds of 2.652(3) Å. $Cu2O_4$ with nearly planar rectangles are characterized by Cu–O distances of 1.896(3) and 1.934(3) Å; the next pair of oxygen atoms is located at 2.983(3) Å.

Table 1 Crystal information and details of X-ray data collection and refinement

Crystal data	
Chemical formula	$K_2(Ca_{0.876}Cu_{0.124})Cu_6O_2(PO_4)_4$
M_r	914.45
Crystal system, space group	Monoclinic, *P*2/*c*
Temperature (K)	293
a, *b*, *c* (Å)	8.3527 (3), 5.6597 (2), 16.8327 (6)
β (°)	94.605 (4)
V (Å^3)	793.18 (5)
Z	2
Radiation type	Mo $K\alpha$
μ (mm^{-1})	9.380
Crystal size (mm)	0.07 × 0.04 × 0.03
Data collection	
Diffractometer	Xcalibur
Absorption correction	Gaussian
T_{min}, T_{max}	0.673, 0.775
No. of measured, independent and observed [$I > 2\sigma(I)$] reflections	6049, 1822, 1471
R_{int}	0.052
$(\sin\theta/\lambda)_{max}$ (Å^{-1})	0.650
Refinement	
$R[F^2 > 2\sigma(F^2)]$, w$R(F^2)$, S	0.038, 0.066, 1.21
No. of reflections	1822
No. of parameters	147
$\Delta\rho_{max}$, $\Delta\rho_{min}$ (e Å^{-3})	1.12, −1.03

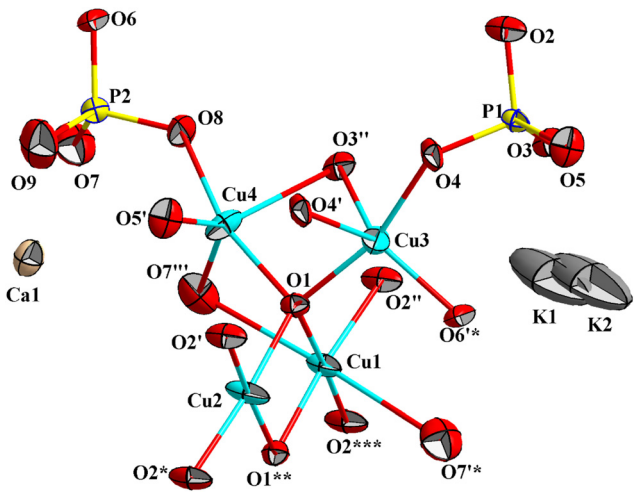

Fig. 2 Independent fragment of the crystal structure of title phase in the ellipsoid mode at the 90% probability level. Symmetry codes: '1 − *x*, 1 − *y*, 1 − *z*; ''1 − *x*, 2 − *y*, 1 − *z*; '''2 − *x*, *y*, 1.5 − *z*; **x*, 1 − *y*, 0.5 + *z*; **1 − *x*, *y*, 1.5 − *z*; ****x*, 2 − *y*, 0.5 + *z*; '*−1 + *x*, *y*, *z*.

Cu3 and Cu4 cations occupy general positions (4g Wyckoff sites) and are coordinated by five oxygen atoms at distances ranging from 1.881(4) to 2.251(3) Å. Additional oxygen atoms are found at 3.194(3) and 2.863(3) Å from Cu3 and Cu4, respectively. All Cu–O bond lengths are typical for divalent copper ions exhibiting pronounced Jahn–Teller distortion. The oxidation states of the copper cations were further confirmed by bond-valence sum (BVS) calculations (Table S3).[21]

Calcium atoms occupy the special 2e Wyckoff site located on a twofold rotation axis. Their coordination environment is octahedral, with Ca–O distances ranging from 2.336(4) to 2.489(4) Å. The large monovalent K^+ ions are eight-coordinated, forming irregular polyhedra with K–O bond lengths between 2.644(5) and 3.534(8) Å.

The framework of the title phase is based on the complex and condensed arrangement of the copper polyhedra. The $Cu1O_6$ octahedra share O1–O1 edges with square-planar $Cu2O_4$ groups to form straight columns extending along the *b* axis (Fig. 3a). These rods are decorated on both sides along the *c* direction by CuO_5 pyramids (Fig. 3b). Pairs of $Cu3O_5$ and $Cu4O_5$ pyramids, which share common edges, are attached to the chains through the same O1 ligands. As a result, each O1 oxygen atom is coordinated exclusively to four copper polyhedra. The $Cu3O_5$ pyramid shares a single vertex O1 with the polyhedra of the rod, whereas the $Cu4O_5$ pyramid shares the O1–O7 edge with a $Cu1O_6$ octahedron (Fig. 3c).

These "decorated" copper ribbons are interconnected by sharing edges between neighboring $Cu3O_5$ pyramids, resulting in the corrugated layers parallel to the *bc* plane. These layers are reinforced with $P1O_4$ tetrahedra, which share all the vertices with copper polyhedra (Fig. 3d). Within this layer, adjacent ribbons alternate their orientation along the *b* axis, directed "up" or "down" as defined by the apical O5 vertex of the $Cu4O_5$ pyramid.

$P2O_4$ tetrahedra link Cu–P blocks into a triperiodic heteropolyhedral framework possessing large channels between blocks (Fig. 4). Two channels run parallel to the *b* axis and one runs along the *c* axis of the unit cell, and they are occupied by slightly disordered K^+ cations (K1 and K2 positions) and smaller Ca^{2+} ions (partially substituted by Cu^{2+} cations).

As mentioned earlier, the O1 oxygen atom is coordinated exclusively by four Cu^{2+} cations, which classifies the new phase as an oxocuprate phosphate. Natural oxocuprate salts, especially arsenates, are widely distributed in fumarolic exhalations, such as at the Tolbachik volcano (Kamchatka Peninsula, Russia). For these structures, the anion-centering approach[22,23] is commonly employed to describe the condensed cationic substructure.

In the crystal structure of $K_2CaCu_6O_2(PO_4)_4$, oxo-centered $[OCu_4]$ tetrahedra are linked *via* shared Cu–Cu edges to form $[O_2Cu_6]^{8+}$ dimers shaped like a bow-knot (Fig. S2). These dimers associate with the $P1O_4$ tetrahedra to create quasi-layers of the type $\{[O_2Cu_6]^{8+}(PO_4)_2\}^{2+}$, called "oxide floors".[24] Along the *a* axis, the oxide floors alternate with "salt floors", $|(K_2Ca)(PO_4)_2|^{2-}$, which consist of large K-centered eightfold polyhedra, CaO_6 octahedra, and $P2O_4$ tetrahedra (Fig. S2 of the SI).

These oxo-centered dimers $[O_2Cu_6]^{8+}$ are the key structural elements in the frameworks of the shchurovskyite structural group, including the title compound, natural oxocuprate arsenates, and synthetic phosphates, as will be discussed further. Similar $[O_2M_8]$ structural units also occur in the family of synthetic oxosalts with the general formula $[M_3O]M(TO_4)_2$ (M = Zn, Cu, and Ni; T = P, As, and V), as reviewed by Bakakin (2025).[24]

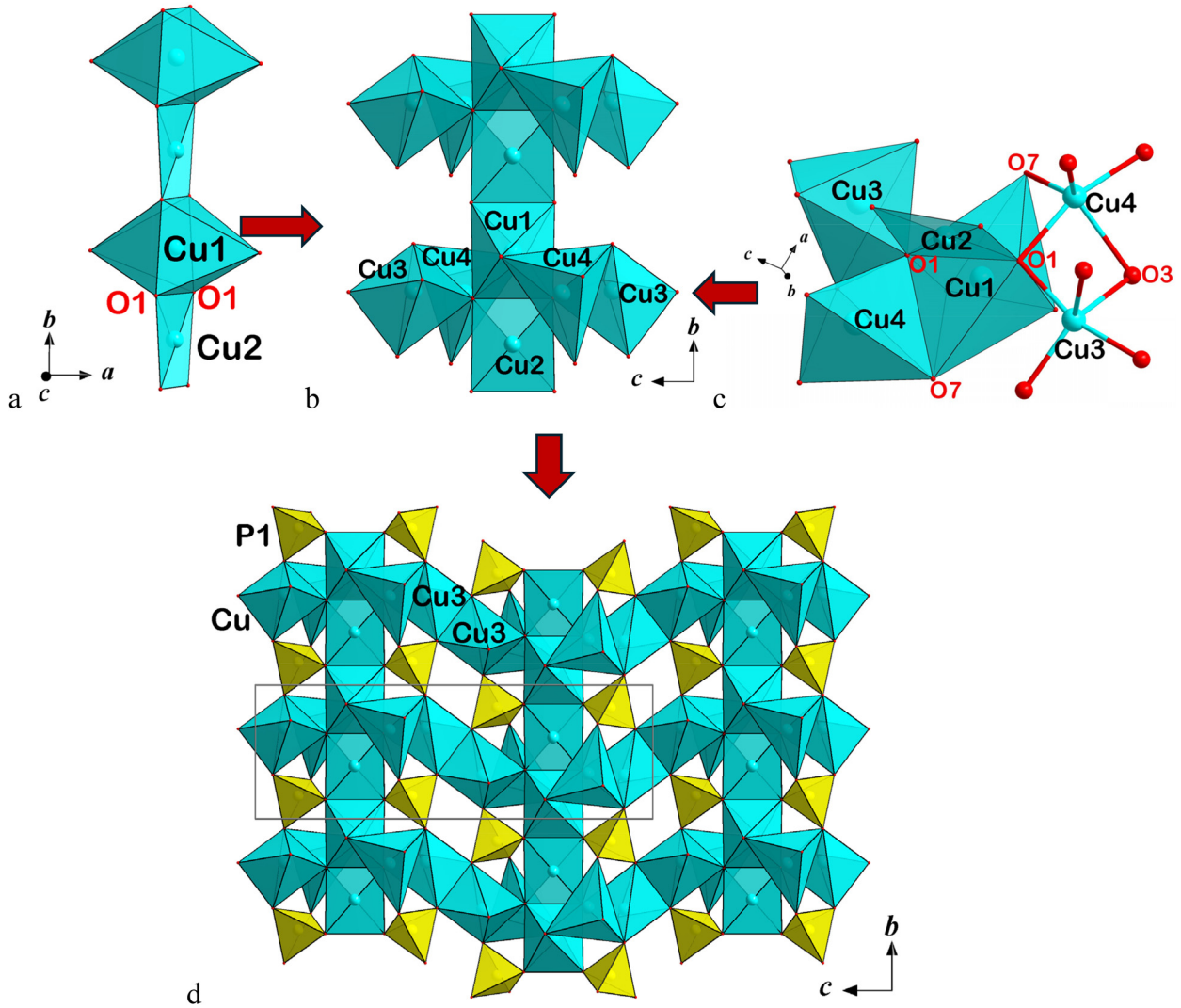

Fig. 3 Structural fragments of the title phase: columns of the $Cu1O_6$ and $Cu2O_4$ polyhedra extended along the *b* axes (a) which are further decorated with the $Cu3O_5$ and $Cu4O_5$ pyramids (b); clusters of copper polyhedra, showing the connectivity between copper polyhedra and coordination for the O1 oxygen atom (c); and heteropolyhedral Cu–P layers (d).

Furthermore, the euchlorine family of natural fumarolic oxocuprate sulfates, comprising puninite, $Na_2[Cu_3O](SO_4)_3$, features crystal structures based on the same $[O_2Cu_6]$ building units.[25] Comparable motifs are also observed in natural and synthetic selenite-chlorides, such as prewittite, $KPb_{0.5}Cu[PbCu_5O_2]Zn(SeO_3)_2Cl_{10}$,[26] and $K[Cu_3O](SeO_3)_2Cl$.[27] Thus, the oxo-centered $[O_2Cu_6]$ dimers demonstrate an exceptional structural versatility, capable of integrating with diverse anionic groups, from phosphates and arsenates to sulfates and selenites. to form a remarkable variety of complex crystal architectures.

Physical properties

Magnetic susceptibility as a function of temperature measurements was performed using a "Quantum Design" MPMS-7T (SQUID) system under an applied field of 0.1 T. Crystals of $K_2CaCu_6O_2(PO_4)_4$ were ground and placed in a gelatin capsule fastened in a plastic straw for immersion into the SQUID system. The specific heat and the isothermal magnetization up to 9 T were measured using a "Quantum Design" PPMS-9T system.

The temperature dependences of dc magnetic susceptibility $\chi_{dc} = M/H$ in $K_2CaCu_6O_2(PO_4)_4$ taken at $\mu_0 H = 0.1$ T in both field-cooled (FC) and zero field-cooled (ZFC) regimes are shown in the main panel of Fig. 5a. These curves practically coincide above the Néel temperature $T_{N1} = 22$ K. At a lower temperature, they slightly diverge and show a rounded hump followed by a sharp increase in the second antiferromagnetic transition at $T_{N2} = 10$ K. The low-temperature phase possesses a weak spontaneous magnetic moment. The inverse dc magnetic susceptibility is shown in Fig. 5b, where the fit by the Curie–Weiss law is shown by the solid line.

To clarify the features of the two-step transition, the *ac* magnetic susceptibility χ_{ac} has been measured at a probing field of

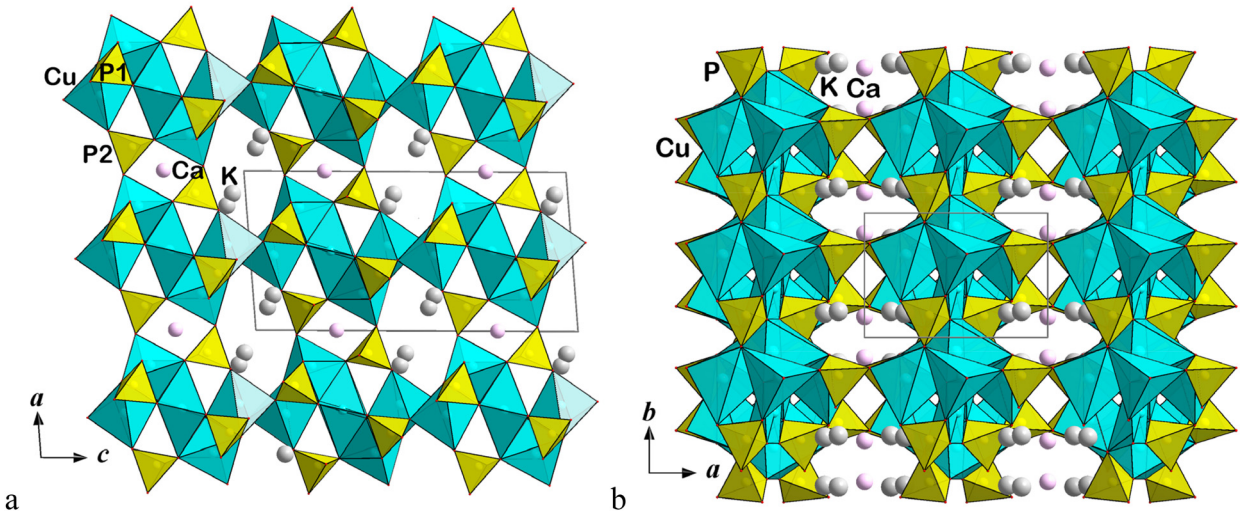

Fig. 4 Crystal framework of the title phase in the *ac* (a) and *ab* (b) projections, showing intercrossing channels filled with K^+ and Ca^{2+} ions.

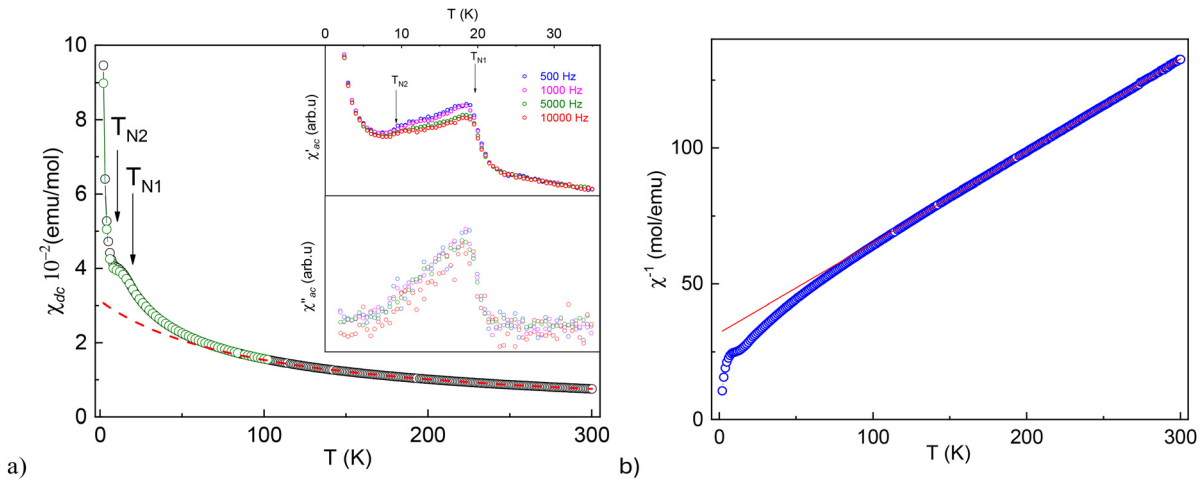

Fig. 5 (a) Temperature dependences of magnetic susceptibility $\chi_{dc}(T)$ in $K_2CaCu_6O_2(PO_4)_4$ under an applied magnetic field of 0.1 T in both FC and ZFC modes. The inset represents both real $\chi'_{ac}(T)$ and imaginary $\chi''_{ac}(T)$ parts of the ac magnetic susceptibility curves at various frequencies. (b) Inverse dc magnetic susceptibility with the fit using the Curie–Weiss law shown by a solid line.

3 Oe in the frequency range $f = 5 \times 10^2$–10^4 Hz, as shown in the inset of Fig. 5. The peak at T_{N1} = 20 K is accompanied by the change in the slope of $\chi'_{ac}(T)$ curves at T_{N2} = 10 K. The positions of these features are not sensitive to the frequency.

Above T_{N1}, the magnetic susceptibility χ_{dc} follows the Curie–Weiss law:

$$\chi = \chi_0 + \frac{C}{T - \Theta} \quad (1)$$

A fit of the $\chi(T)$ data in the 200–300 K temperature interval gives a temperature-independent diamagnetic contribution $\chi_0 = -(2.1 \pm 0.9) \times 10^{-4}$ emu mol^{-1}, the Weiss temperature Θ = −98 ± 4 K and the Curie constant $C = 3.08 \pm 0.06$ emu K mol^{-1}. The negative value of Weiss temperature points to dominant antiferromagnetic interactions between the Cu^{2+} cations. From the Curie constant, the effective magnetic moment per formula unit is as follows:

$$\mu_{eff} = (8C)^{1/2}\mu_B, \quad (2)$$

which is calculated to be $\mu_{eff} = 4.96\mu_B$. This value is higher than the spin-only moment, $\mu_{eff}^{calc} = 4.24\mu_B$, expected for six ($n = 6$) Cu^{2+} ($S = 1/2$) ions per formula unit. The experimentally found *g*-factor, $g = 2.32$, stems from the value of the Curie constant through the ratio as follows:

$$8C = ng^2S(S+1), \quad (3)$$

This value is typical for Cu^{2+} systems with substantial spin–orbit coupling. $K_2CaCu_6O_2(PO_4)_4$ stands out by the rich variety of the local environment of copper ions. The CuO_4, CuO_5 and CuO_6 units can be separated in this compound. It means that

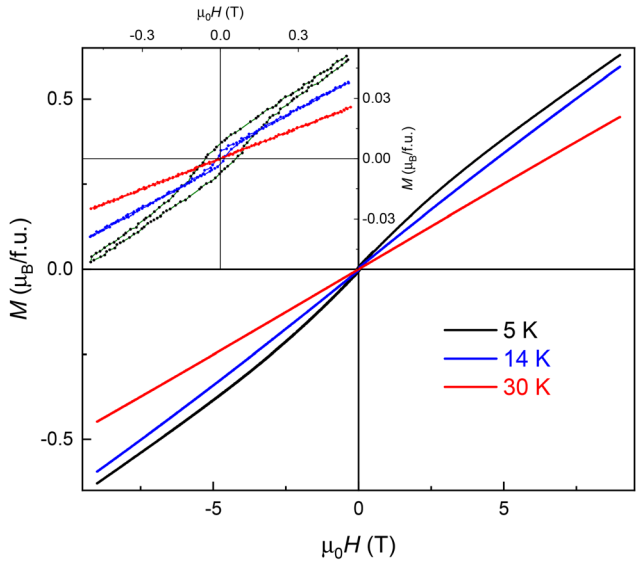

Fig. 6 Field dependences of magnetization in $K_2CaCu_6O_2(PO_4)_4$ at various temperatures. Inset: the enlarged fragment of the $M(H)$ curve.

the spin–orbit coupling and the g-factor of Cu^{2+} ions may vary within wide limits.[28]

The field dependence of magnetization taken at T = 2 K is shown in Fig. 6. At $\mu_0 H$ = 7 T, the magnetization reaches a value of 0.5μ_B, which indicates that the system is far from the saturation. The calculated saturation magnetization M_{sat} is about 7μ_B. The weak hysteresis loop is visible for $T < T_{N1}$ (inset of Fig. 6).

The presence of two subsequent magnetic transitions was confirmed by specific heat measurement, as shown in Fig. 7. The singularities barely seen in the $C_p(T)$ curve (inset of Fig. 7) are better pronounced in C_p/T *vs.* T^2 presentation at T_{N1} = 22 K and T_{N2} = 11 K, which is consistent with the magnetic susceptibility data. Low magnitudes of these anomalies may be due to the fact that most part of the magnetic entropy is released at much higher temperatures. It should be noted that the experimental data on magnetic susceptibility start deviating from the extrapolation of the Curie–Weiss fit at about 85 K. The C_p/T *versus* T^2 data allow identifying the phase transitions at T_{N1} and T_{N2} because in this representation, the lattice contribution at low temperatures is linear. The deviations from linearity correspond to magnetic contribution.

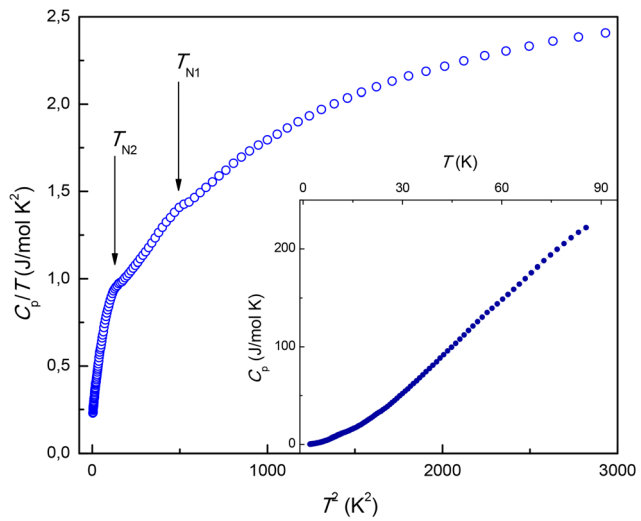

Fig. 7 C_p/T *vs.* T^2 plot for $K_2CaCu_6O_2(PO_4)_4$. Inset: temperature dependence of specific heat C_p.

The relation between two main thermodynamic properties, *i.e.*, magnetization and specific heat, stems from Boltzmann statistics. It has been shown by a general theoretical argument that the variation in the magnetic specific heat of a 'simple' antiferromagnet, in particular the singular behavior in the region of transition, should be closely similar to the behavior of the function $\partial(\chi T)\partial T$, where χ is the zero-field susceptibility.[29] The positions of singularities in Fisher's specific heat, $d(\chi T)/dT$, are seen at T_{N1} = 22 K and T_{N2} = 10 K, as shown in Fig. S3 of the SI.

The transitions at T_{N1} and T_{N2} are of different natures. At T_{N1}, the system transforms from paramagnetic into magnetically ordered state with spontaneous magnetization. This transition is well pronounced in both real χ'_{ac} and imaginary χ''_{ac} parts of the ac magnetic susceptibility, as shown in the inset of Fig. 5. At T_{N2}, the transition occurs between two magnetically ordered states. Contrary to the real part of ac susceptibility, the imaginary part does not evidence any anomalies at T_{N2}. It means that no significant dissipation processes accompany this transition. This is in line with the observation that both phases at $T < T_{N2}$ and $T_{N2} < T < T_{N1}$ possess similar properties, *i.e.* the presence of a small uncompensated moment and the hysteresis loop, as shown in the inset of Fig. 6.

Crystal chemistry of the shchurovskyite family of compounds

As it was mentioned earlier, the title oxocuprate phosphate, $K_2CaCu_6O_2(PO_4)_4$, represents a new synthetic modification of the natural fumarolic arsenate shchurovskyite $K_2CaCu_6O_2(AsO_4)_4$.[13] Both phases exhibit similar crystal structures, which is reflected in their closely comparable unit-cell parameters and volumes (Table 2). Nevertheless, the title phase crystallizes in the centrosymmetric space group $P2/c$, in contrast to the polar $C2$ structure of shchurovskyite, indicating that $K_2CaCu_6O_2(PO_4)_4$ corresponds to a new structure type.

Beyond these two compounds, several additional synthetic and natural phases have been assigned to the shchurovskyite-related structural family. Although mostly non-isostructural, all of them conform to the general formula $A_2B[M_6O_2](TO_4)_4$, where A is monovalent large alkali cation K^+ or Rb^+; B is primarily Ca^{2+} but in some cases Cu^{2+} or K^+; T is P or As; M is Cu, or a combination of Cu and Al.

Within this family, only one isostructural-to-shchurovskyite synthetic phase was obtained – the Rb-substituted phosphate, $Rb_2Ca[Cu_6O_2](PO_4)_4$.[14] A second mineral in this group, dmisokolovite, $K_2K[Cu_5AlO_2](AsO_4)_4$, was discovered together with shchurovskyite in Arsenatnaya fumarole sublimates.[13] Interestingly, its composition is notable for containing only K^+

Table 2 Crystallographic parameters, structural characteristics and synthesis data of shchurovskyite-related salt-inclusion oxocuprates $A_2B[M_6O_2](TO_4)_4$

Formula	Space group, Z, V (Å^3)	Unit-cell parameters, (Å and °)	Cu-layers characteristics	Genesis/synthesis conditions	Ref.
Shchurovskyite, $K_2Ca[Cu_6O_2](AsO_4)_4$	$C2$ 2 839.24(9)	a 17.2856(9) b 5.6705(4), β 92.953(6) c 8.5734(6)	Columns of CuO_4 and CuO_6 Decoration with CuO_5 Vertice connection	Sublimates of Arsenatnaya fumarole at temperatures above 380 °C	13
$Rb_2Ca[Cu_6O_2](PO_4)_4$	$C2$ 2 794.57(4)	a 16.8913(4) b 5.6406(4), β 93.919(3) c 8.3591(3)	Columns of CuO_4 and CuO_6 Decoration with CuO_5 Vertice connection	Hydrothermal synthesis at 420 °C	14
$K_2Ca[Cu_6O_2](PO_4)_4$	$P2/a$[a] 2 793.18(5)	a 16.8327(6) b 5.6597(2), β 94.605(4) c 8.3527(3)	Columns of CuO_4 and CuO_6 Decoration with CuO_5 Edge connection	Flux in KCl at 690 °C	This paper
Dmisokolovite, $K_3[Cu_5AlO_2](AsO_4)_4$	$C2/c$ 4 1614.7(2)	a 17.0848(12) b 5.7188(4), β 91.716(6) c 16.5332(12)	Columns of CuO_4 and AlO_6 Decoration with CuO_5 Vertice connection	Sublimates of Arsenatnaya fumarole at temperatures above 380 °C	13
$K_2Cu[Cu_6O_2](PO_4)_4$	$P\bar{1}$[b] 1 382.58(3)	a 8.2612(4), α 103.239(4) b 5.7787(3), β 95.813(4) c 8.3717(4), γ 96.821(4)	Columns of CuO_5 Decoration with CuO_5 and CuO_6 Edge connection	Gas-phase crystallization at 800 °C	15
$K_{2.35}Cu_{0.825}[Cu_6O_2](PO_4)_4$	$P2_1/n$ 8 3172.47(13)	a 16.7138(4) b 11.2973(3), β 90.775(2) c 16.8031(4)	Columns of CuO_5 Decoration with CuO_5 and CuO_6 Edge connection	Gas-phase crystallization at 800 °C	15

[a] Standard setting $P2/c$ was converted to $P2/a$ for convenient comparison between polymorphs. [b] The authors setting was changed for the same reason.

cations (rather than both K^+ and Ca^{2+}), with charge balance maintained by the substitution of Cu^{2+} for Al^{3+}. The crystal framework of dmisokolovite was shown to be a derivative to that of shchurovskyite.[13] Additionally, two more shchurovskyite-related compounds have recently been synthesized by gas-phase crystallization under conditions emulating natural fumarolic environments: triclinic $K_2Cu[Cu_6O_2](PO_4)_4$ and monoclinic $K_{2.35}Cu_{0.825}[Cu_6O_2](PO_4)_4$.[15] The relationships among these phases – considering archetypes and derivative superstructures that correlate with Z and unit-cell volumes – were comprehensively outlined by Kornyakov and Krivovichev.[15]

As shown in Table 2, all members of the shchurovskyite family differ primarily in the salt part of their structures, while sharing very similar compositions and cationic substructures within the "oxide floor" fragments $\{[O_2M_6]^{8+}(TO_4)_2\}$. Nevertheless, the anionic environment of the copper polyhedra varies together with the changes in symmetry, which is clearly illustrated by the Cu-layer slices of the frameworks in Fig. 8.

Both centrosymmetric synthetic $K_2CaCu_6O_2(PO_4)_4$ (Fig. 8a) and polar natural shchurovskyite $K_2CaCu_6O_2(AsO_4)_4$ (Fig. 8b) contain the same columns built of alternating CuO_4 planar squares and CuO_6 octahedra in their structures. However, differences emerge in the orientation and connectivity of the copper pyramids that decorate these rods. In the synthetic phosphate, the $Cu4O_5$ pyramids alternate the orientation of their O5 apical vertices (up/down) along the b axis in adjacent ribbons. In contrast, analogous $Cu2O_5$ pyramids in shchurovskyite maintain a single orientation, contributing to the polar character of the layer. The same polarity is reinforced by the second type of $Cu1O_5$ pyramids, which share only one vertex (O1) with each other. In the synthetic modification, this pyramid is slightly twisted, resulting in edge-sharing (O4–O4) connections between neighboring $Cu3O_5$ pyramids.

In crystal structures of the other two synthetic compounds – triclinic $K_2Cu[Cu_6O_2](PO_4)_4$ (Fig. 8c) and monoclinic $K_{2.35}Cu_{0.825}[Cu_6O_2](PO_4)_4$ (Fig. 8d) – the columns consist entirely of CuO_5 pyramids (here and below, only Cu–O bonds ≤2.9 Å are considered). Remarkably, the orientation of these pyramids was shown to form different sequences: UDUDUD for $K_2Cu[Cu_6O_2](PO_4)_4$ and UUDDUU for $K_{2.35}Cu_{0.825}[Cu_6O_2](PO_4)_4$, where U and D denote apical vertices pointing upward or downward relative to the plane of the copper layer.[15] Furthermore, the combination of pyramids and octahedra contributes additional "decoration" to the columns – whereas in all other structures of the shchurovskyite family, only pyramids play this role (Table 2). At the same time, the decorating pyramids in the synthetic phases are linked by edge-sharing, in contrast to the vertex-sharing connectivity typical of the natural phases and the Rb-containing isostructural analogue. This edge-sharing pattern is consistent with centrosymmetric structures, while vertex-sharing is associated with the polar frameworks of minerals (Table 2).

Thus, most monoclinic shchurovskyite-related compounds crystallize in different space groups and structure types. This pronounced structural flexibility stems from the strong tendency of Cu^{2+} polyhedra to undergo Jahn–Teller distortions, which promote structural rearrangements driven by temperature effects and compositional variations.

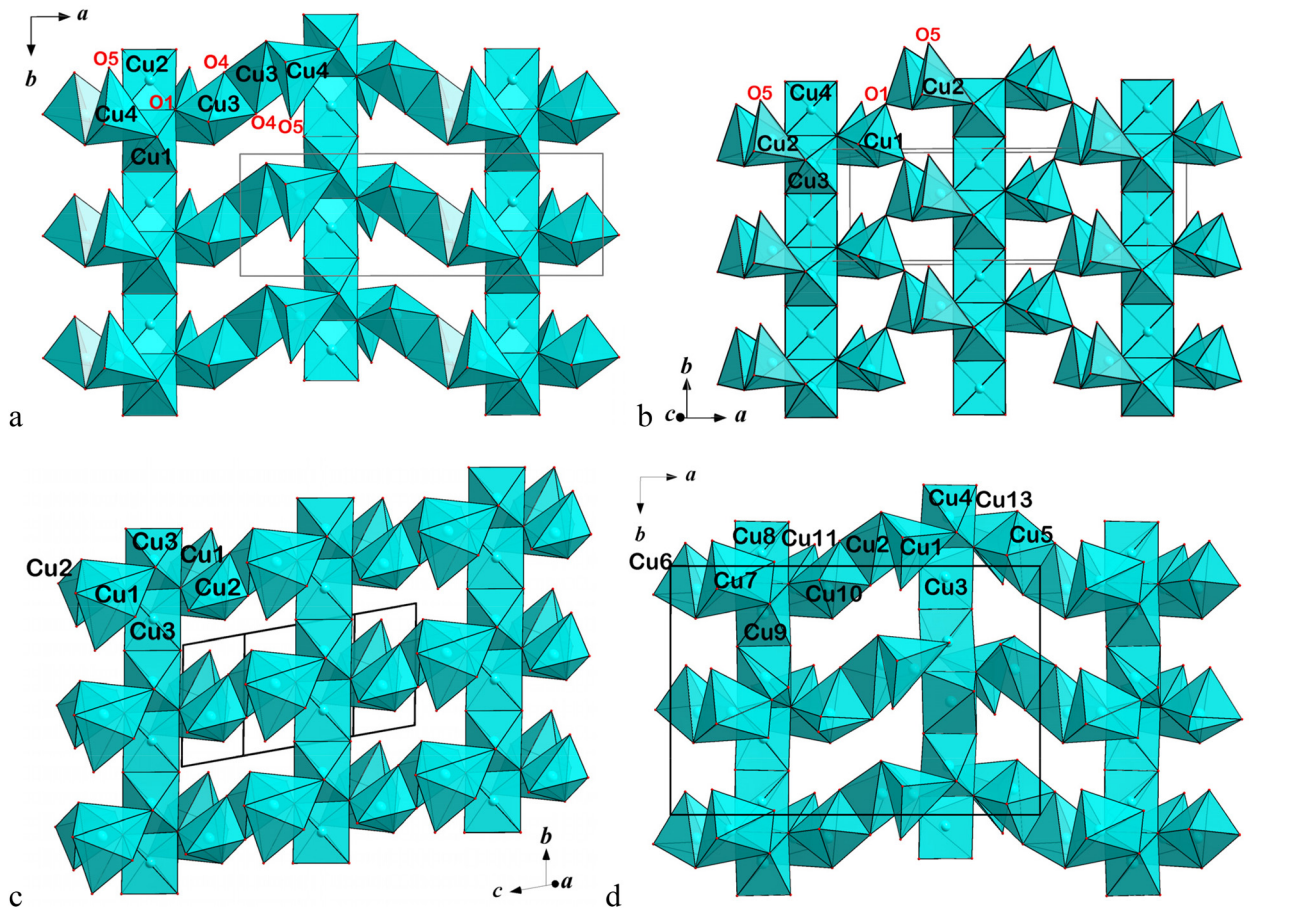

Fig. 8 Layers built by the copper polyhedra in the crystal structures of $K_2CaCu_6O_2(PO_4)_4$, space group $P2/a$[a] (a); shchurovskyite, $K_2CaCu_6O_2(AsO_4)_4$, sp. gr. $C2$ (b); $K_2CuCu_6O_2(PO_4)_4$, sp. gr. $P\bar{1}$[b] (c) and $K_{2.35}Cu_{0.825}Cu_6O_2(PO_4)_4$, sp. gr. $P2_1/n$ (d). [a,b]Settings as in Table 2.

Large channels accommodating K^+ ions run along the b axis through the framework of $K_2CaCu_6O_2(PO_4)_4$ (Fig. 4a). The channels are framed with four copper pyramids and four phosphate tetrahedra alternating with each other. The effective width of the channel[30] is 2.5 Å × 5.2 Å (the smallest O8–O8 and the longest O4–O4 distances, respectively), suggesting easy migration of K^+ ions through the structure. Thus, we made calculations of potential migration paths for K^+ ions based on the structural topology by means of the ToposPro program[31] and evaluated the energy barriers using the bond-valence energy landscape algorithm,[32] as shown in Fig. 9, using the VESTA software.[33] For the topological calculations, based on the Voronoi-Dirichlet partition, the threshold values were established as follows: r_{sd} = 1.70 Å and r_{chan} = 2.38 Å, which derive from the sizes of K^+ and O^{2-} ions.[34] As a result, the 1D paths for K^+ ions were established running along the b axis through the large channels, described above. The BVEL calculations based on structural data confirmed the probability of K^+ migration through the crystal structure, which can occur along the b axis at 0.6 eV (Fig. 9).

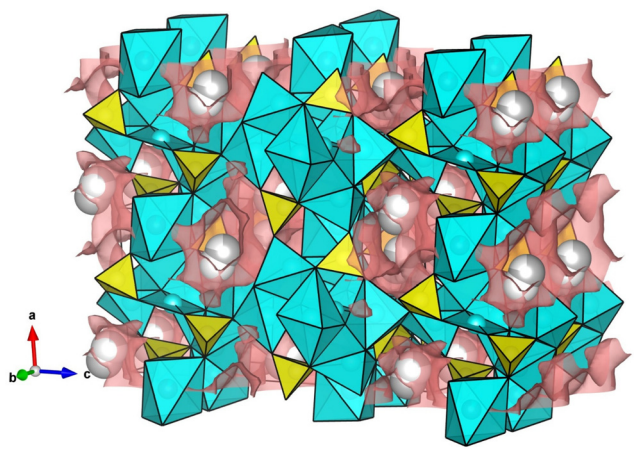

Fig. 9 Bond-valence energy landscape isosurfaces (isosurface level 15) for potassium atoms in the $K_2CaCu_6O_2(PO_4)_4$ structure shown in axonometric projection.

Summary

Single crystals of a new shchurovskyite-like oxocuprate phosphate, $K_2CaCu_6O_2(PO_4)_4$, were obtained *via* a flux method. Its

crystal structure features rods composed of alternating CuO_6 and CuO_4 polyhedra, sharing edges. These rods are decorated by CuO_5 pyramids. In contrast to the vertex-sharing connectivity typical of the shchurovskyite and its Rb-analogue, $Rb_2Ca[Cu_6O_2](PO_4)_4$, the decorating pyramids show the title-phase edge-sharing. This difference in polyhedral linkage correlates with a significant variation in the copper–copper distances between decorated pyramids of neighboring rods: Cu3–Cu3 = 3.194 Å (K) *vs.* Cu1–Cu1 = 3.760 Å (Rb). Our study once again demonstrated the flexibility of the shchurovskyite structural archetype. This flexibility is governed by modifications to the "salt" part of the structure, in contrast to the conserved cationic substructure of the $\{[O_2M_6]^{8+}(TO_4)_2\}$ "oxide-floor". The main variations occur principally in the "salt" cation sites, correlating with the changes in geometry and/or the connectivity of Jahn–Teller-active Cu^{2+} polyhedra. Bond-valence energy landscape calculations based on structural data confirmed the assumed probability of K^+ migration through the crystal structure along the *b* axis at 0.6 eV.

Recently, it has been shown that $Rb_2Ca[Cu_6O_2](PO_4)_4$ orders ferrimagnetically at T_C = 25 K and evidences a 1/3 magnetization plateau starting at the zero magnetic field. It is because in the anion-centered $[O_2Cu_6]$ dimer of the Rb-based compound (see Fig. 6a of ref. 14), the collinear UUDDUU spin state (U = up, D = down) is realized due to the competition of purely antiferromagnetic exchange interactions. The density functional theory calculations of super-exchange parameters in $Rb_2CaCu_6O_2(PO_4)_4$ point to the possible low-dimensional magnetic behavior of this compound, since they confirm weak magnetic coupling between the Cu-based layers. However, the actual character of the low-dimensional magnetism (1D or 2D) remains uncertain, owing to the presence of weak exchange interactions within the layers. Experimentally found value of the most intense component of the *g*-tensor reach $g = 2.31 \pm 0.01$, which is in good correspondence with the calculated value and the value of *g*-factor $g = 2.32$ found in $K_2CaCu_6O_2(PO_4)_4$. The low-dimensional magnetic behavior of $Rb_2CaCu_6O_2(PO_4)_4$ is masked by the fierce competition between multiple ferromagnetic and antiferromagnetic exchange interactions.

Contrary to these observations, $K_2CaCu_6O_2(PO_4)_4$ appears to be canted antiferromagnet with weaker spontaneous magnetization most probably due to the Dzyaloshinskii–Moriya interaction. The K-based compound orders at two steps at T_{N1} = 22 ± 2 K and T_{N2} = 10 ± 1 K, where T_{N1} corresponds to the onset of the long-range magnetic order, while the transition at T_{N2} corresponds to some rearrangement of the magnetic structure. Notably, weak spontaneous magnetization is present at both $T_{N2} < T < T_{N1}$ and $T < T_{N2}$ ranges. The magnetic structures in these temperature ranges can be established in the neutron scattering experiments.

Conflicts of interest

There are no conflict to declare.

Data availability

Supplementary information (SI) is available: XRPD (Fig. S1), atomic coordinates (Table S1), interatomic distances (Table S2), bond-valence data (Table S3), the anio-centering projection of the title compound' crystal structure (Fig. S2), and the temperature dependence of Fisher's specific heat (Fig. S3). See DOI: https://doi.org/10.1039/d6dt00109b.

CCDC 2505942 for $K_2CaCu_6O_2(PO_4)_4$ contains the supplementary crystallographic data for this paper.[35]

Acknowledgements

We thank N. V. Zubkova for her assistance in obtaining the X-ray diffraction data set. We are grateful to V. O. Yapaskurt for the X-ray spectral analysis. This work has been supported by Lomonosov Moscow State University (award no. AAA-A16-116033010121-7) and by the Ministry of Science and Higher Education of the Russian Federation within the framework of the Priority-2030 strategic academic leadership program at NUST MISIS. G. K. is grateful for the FMUF-2022-0002 state research project of IEM RAS. Access to the powder diffractometer Tongda-TDM-20 (Geology Faculty) was granted by the Lomonosov Moscow State University Program of Development.

References

1 I. V. Pekov, AA Agakhanov, N. V. Zubkova, N. N. Koshlyakova, N. V. Shchipalkina, F. D. Sandalov, V. O. Yapaskurt, A. G. Turchkova and E. G. Sidorov, *Russ. Geol. Geophys.*, 2020, **61**(5–6), 675–688.
2 F. Pertlik and J. Zemann, *Mineral. Petrol.*, 1988, **38**(4), 291–298.
3 V. R. Popova, V. A. Popov, N. S. Rudashevskiy, S. F. Gravatskikh, V. O. Polyakov and A. F. Bushsmakin, *Zap. Vses. Mineral. O-va.*, 1987, **116**, 358–367. (in Russian).
4 I. V. Pekov, S. N. Britvin, A. A. Agakhanov, M. F. Vigasina and E. G. Sidorov, *Eur. J. Mineral.*, 2019, **31**(5–6), 1025–1032.
5 A. Vasiliev, O. Volkova, E. Zvereva and M. Markina, *npj Quantum Mater.*, 2018, **3**(1), 18.
6 G. L. Starova, S. K. Filatov, V. S. Fundamensky and L. P. Vergasova, *Mineral. Mag.*, 1991, **55**(381), 613–616.
7 V. Y. Pomjakushin, A. Podlesnyak, A. Furrer and E. V. Pomjakushina, *Phys. Rev. B*, 2024, **109**(14), 144409.
8 M. Fujihala, T. Sugimoto, T. Tohyama, S. Mitsuda, R. A. Mole, D. H. Yu, S. Yano, Y. Inagaki, H. Morodomi, T. Kawae, H. Sagayama, R. Kumai, Y. Murakami, K. Tomiyasu, A. Matsuo and K. Kindo, *Phys. Rev. Lett.*, 2018, **120**(7), 077201.
9 A. N. Vasiliev, O. S. Volkova, E. A. Zvereva, A. V. Koshelev, V. S. Urusov, D. A. Chareev, V. I. Petkov, M. V. Sukhanov, B. T. Rahaman and B. T. Saha-Dasgupta, *Phys. Rev. B: Condens. Matter Mater. Phys.*, 2015, **91**(14), 144406.

10 D. I. Badrtdinov, E. S. Kuznetsova, V. Y. Verchenko, P. S. Berdonosov, V. A. Dolgikh, V. V. Mazurenko and A. A. Tsirlin, *Sci. Rep.*, 2018, **8**(1), 2379.
11 H. C. Wu, K. N. Denisova, D. Menzel, D. C. Kakarla, O. V. Maximova, T. W. Kuo, Z. H. Yang, C. H. Lee, W. H. Li, H. Berger, C. W. Wang, C. K. Chang, Y. C. Chuang, J.-Y. Lin, M. Gooch, C. W. Chu, A. N. Vasiliev and H. D. Yang, *Phys. Rev. B*, 2019, **100**(24), 245119.
12 A. S. Botana, H. Zheng, S. H. Lapidus, J. F. Mitchell and M. R. Norman, *Phys. Rev. B*, 2018, **98**(5), 054421.
13 I. V. Pekov, N. V. Zubkova, D. I. Belakovskiy, V. O. Yapaskurt, M. F. Vigasina, E. G. Sidorov and D. Y. Pushcharovsky, *Mineral. Mag.*, 2015, **79**, 1737–1753.
14 S. M. Aksenov, E. Y. Borovikova, V. S. Mironov, N. A. Yamnova, A. S. Volkov, D. A. Ksenofontov, O. A. Gurbanova, O. V. Dimitrova, D. V. Deyneko, E. A. Zvereva, O. V. Maximova, S. V. Krivovichev, P. C. Burns and A. N. Vasiliev, *Acta Crystallogr., Sect. B:Struct. Sci., Cryst. Eng. Mater.*, 2019, **75**, 903–913.
15 I. V. Kornyakov and S. V. Krivovichev, *Crystals*, 2021, **11**, 807.
16 Agilent Technologies, *CrysAlis PRO*, Yarnton, UK, 2014.
17 G. M. Sheldrick, *Acta Crystallogr., Sect. A:Found. Adv.*, 2015, **71**, 3–8.
18 G. M. Sheldrick, *Acta Crystallogr., Sect. C:Struct. Chem.*, 2015, **71**, 3–8.
19 L. J. Farrugia, *J. Appl. Crystallogr.*, 2012, **45**, 849–854.
20 K. Brandenburg, *DIAMOND*, Crystal Impact GbR, Bonn, Germany, 2006.
21 I. D. Brown and D. Altermatt, *Acta Crystallogr., Sect. B: Struct. Sci.*, 1985, **41**, 244–247.
22 S. V. Krivovichev and S. K. Filatov, *The Crystal Chemistry of Inorganic Compounds and Minerals that Contain Radicals of Anion-Centered Tetrahedra*, St. Petersburg University, 2001.
23 S. V. Krivovichev, O. Mentre, O. I. Siidra, M. Colmont and S. K. Filatov, *Chem. Rev.*, 2013, **113**(8), 6459–6535.
24 V. V. Bakakin, *J. Struct. Chem.*, 2025, **66**, 1491–1526.
25 O. I. Siidra, E. V. Nazarchuk, A. N. Zaitsev, E. A. Lukina, E. Y. Avdontseva, L. P. Vergasova, N. S. Vlasenko, S. K. Filatov, R. Turner and G. A. Karpov, *Eur. J. Mineral.*, 2017, **29**, 499–510.
26 R. R. Shuvalov, L. P. Vergasova, T. F. Semenova, S. K. Filatov, S. V. Krivovichev, O. I. Siidra and N. S. Rudashevsky, *Am. Mineral.*, 2013, **98**, 463–469.
27 V. M. Kovrugin, M. Colmont, O. Mentré, O. I. Siidra and S. V. Krivovichev, *Mineral. Mag.*, 2016, **80**, 227–238.
28 S. A. Al'tshuler and B. M. Kozyrev, *Electron paramagnetic resonance*, Academic Press, 2013.
29 M. E. Fisher, *Philos. Mag.*, 1962, **7**, 1731–1743.
30 L. McCusker, F. Liebau and G. Engelhardt, *Microporous Mesoporous Mater.*, 2003, **58**, 3–13.
31 V. A. Blatov, A. P. Shevchenko and D. M. Proserpio, *Cryst. Growth Des.*, 2014, **14**, 3576.
32 BVlain Python Package, available at: https://github.com/dembart/BVlain (accessed December 2024).
33 K. Momma and F. Izumi, *J. Appl. Crystallogr.*, 2008, **41**, 653–658.
34 V. A. Blatov, *Crystallogr. Rev.*, 2004, **10**, 249.
35 CCDC 2505942: Experimental Crystal Structure Determination, 2026, DOI: 10.25505/fiz.icsd.cc2q3mvb.